

A Simple Route to Reduced Graphene Oxide-Draped Nanocomposites with Markedly Enhanced Visible-Light Photocatalytic Performance

Xueqin Liu, Jianbo Yang, Wen Zhao, Yang Wang, Zhen Li,* and Zhiqun Lin*

Nanocomposites (denoted RGO/ZnONRA) comprising reduced graphene oxide (RGO) draped over the surface of zinc oxide nanorod array (ZnONRA) were produced via a simple low-temperature route, dispensing with the need for hydrothermal growth, electrochemical deposition or other complex treatments. The amount of deposited RGO can be readily tuned by controlling the concentration of graphene oxide (GO). Interestingly, the addition of Sn²⁺ not only enables the reduction of GO, but also functions as a bridge that connects the resulting RGO and ZnONRA. Remarkably, the incorporation of RGO improves the visible-light absorption and reduces the bandgap of ZnO, thereby leading to the markedly improved visible-light photocatalytic performance. Moreover, RGO/ZnONRA nanocomposites exhibit a superior stability as a result of the surface protection of ZnONRA by RGO. The mechanism on the improved photocatalytic performance based on the cophotosensitizations under the visible-light irradiation has been proposed. This simple yet effective route to the RGO-decorated semiconductor nanocomposites renders the better visible-light utilization, which may offer great potential for use in photocatalytic degradation of organic pollutants, solar cells, and optoelectronic materials and devices.

1. Introduction

Because of its direct wide bandgap of 3.37 eV and high electron mobility, zinc oxide (ZnO) has been extensively used in photocatalysis and photovoltaics.^[1–4] In comparison to ZnO nanoparticles, ZnO nanorod arrays (ZnONRA) possess several advantageous attributes. First, the precise 1D

orientation of ZnONRA with less grain boundary provides a vectorial pathway for the electron transport and thus reduces the recombination of electron–hole pairs. Second, the light absorption is largely enhanced due to the multiple internal reflections between adjacent ZnO nanorods. Finally, it is convenient to reuse and recover ZnO nanorods as they are directly grown on the substrate.^[5–7] However, the low quantum yield and the lack of the visible-light utilization restrict the practical applications of ZnONRA. To this end, ZnONRA have been modified with noble metals, semiconductor nanoparticles, and carbon materials to alleviate these problems.^[8–10]

As a 2D honeycomb carbon sheet, reduced graphene oxide (RGO) has attracted much attention due to its superior electronic mobility, remarkable optical transmittance, excellent chemical stability, and high specific surface area, conferring it for a rich variety of applications, including sensors, interconnects, and energy conversion and storage.^[11–16] Recently, RGO-based nanocomposites have emerged as a

X. Q. Liu, J. B. Yang, W. Zhao, Y. Wang, Prof. Z. Li
Faculty of Materials Science and Chemistry
China University of Geosciences
Wuhan, Hubei 430074, China
E-mail: zhenli@cug.edu.cn

X. Q. Liu, Prof. Z. Q. Lin
School of Materials Science and Engineering
Georgia Institute of Technology
Atlanta, GA 30332, USA
E-mail: zhiqun.lin@mse.gatech.edu



DOI: 10.1002/sml.201601110

promising material for a new class of functional devices, which can greatly enhance photocatalytic performance due to high adsorption of organic pollutants because of the large surface area of composites and the π - π interactions between aromatic of RGO and organic pollutants, the increased absorption intensity of incident light and extended light absorption range, and the effective charge transfer owing to the high charge-carrier mobility of RGO.^[17–19] To date, RGO/ZnO nanocomposites prepared by combining ZnO nanoparticles and RGO have been reported.^[20–22] However, the attempts to produce nanocomposites consisting of ZnO nanorod arrays and RGO are comparatively few and limited in scope.^[23–25] It is notable that in these studies the hydrothermal growth, electrochemical deposition, and other complex approaches were employed, and they primarily focused on the growth of ZnONRA on the surface of RGO for use in solar cells^[26,27] and hybrid photodetector.^[28–30]

Herein, we report, for the first time, an extremely simple yet highly effective low-temperature wet-chemistry deposition route to producing the RGO/ZnONRA nanocomposites for application in visible-light photocatalytic degradation with markedly enhanced performance over the ZnONRA alone. The amount of RGO draped over the surface of ZnONRA can be readily modulated by changing the concentration of graphene oxide (GO). It is interesting to note that the addition of Sn^{2+} facilitates the reduction of GO and bridges the resulting RGO and the ZnONRA. More importantly, the incorporation of RGO reduces the bandgap of ZnO and thus renders the greatly improved photocatalytic degradation performance of organic pollutants under the visible-light irradiation. Owing to the presence of RGO as the surface protection of ZnONRA, the RGO/ZnONRA nanocomposites exhibited an excellent stability.

2. Results and Discussion

The RGO sheets were deposited on the surface of ZnONRA via a simple yet robust wet-chemistry approach (see the Experimental Section). The crystal phases and orientation of as-synthesized GO, ZnONRA, and RGO/ZnONRA nanocomposites were analyzed by X-ray powder diffraction (XRD) (Figure 1). GO showed a sharp diffraction peak at $2\theta = 10.8^\circ$, corresponding to the reflection of the (001) crystalline plane.^[31] The ZnONRA exhibited the diffraction peaks at $2\theta = 31.4^\circ$, 34.0° , 35.9° , and 47.2° , suggesting the formation of wurtzite phase of ZnO (JCPDS Card No. 36–1451; space group $P6_3mc$, $a = 3.24982 \text{ \AA}$, $c = 5.20661 \text{ \AA}$). Two additional peaks at $2\theta = 43.63^\circ$ and 50.79° were resulted from the diffraction of the alloyed Fe–Co–Ni substrate. Clearly, the intensity of the (002) peak of ZnO at $2\theta = 34.0^\circ$ is much higher than the other peaks, signifying that ZnO nanorods were preferentially oriented in the c -axis direction (i.e., perpendicular to the substrate).^[32] The XRD patterns of three RGO/ZnONRA nanocomposites (i.e., RGO/ZnONRA-1, RGO/ZnONRA-2 and RGO/ZnONRA-3) were similar to that of as-prepared ZnONRA. Notably, the diffraction peak of GO in the RGO/ZnONRA nanocomposites completely disappeared, suggesting the successful reduction of GO by Sn^{2+}

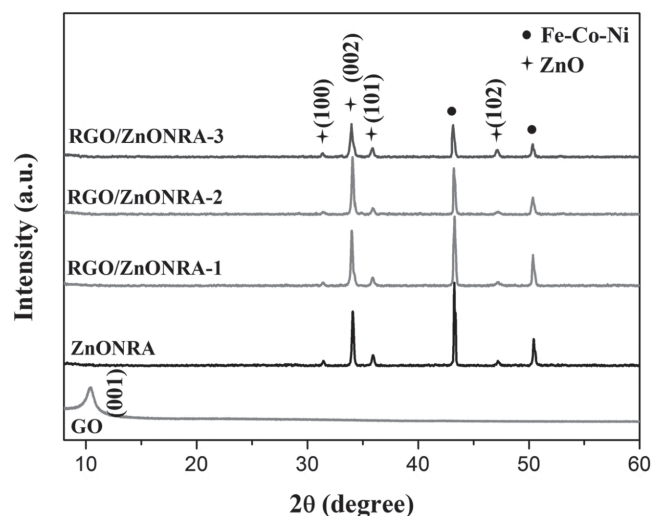


Figure 1. XRD patterns of GO, ZnONRA, and RGO/ZnONRA nanocomposites synthesized at different amounts of RGO (i.e., RGO/ZnONRA-1 at the concentration of GO, $c = 0.5 \text{ mg mL}^{-1}$, RGO/ZnONRA-2 at $c = 2 \text{ mg mL}^{-1}$, and RGO/ZnONRA-3 at $c = 8 \text{ mg mL}^{-1}$, respectively).

to yield nanocomposites. No characteristic diffraction peaks of RGO were seen due primarily to the ultrathin thickness of RGO compared to ZnO nanorods and the fine dispersion of RGO sheets on the nanocomposites. The absence of the diffraction peaks of SnO_2 implied its removal during the washing process of nanocomposites (see the Experimental Section). It is interesting to note that the peak intensities of ZnO decreased progressively with the increased amount of RGO deposited, which can be ascribed to the shielding effect of RGO on the surface of ZnONRA.

The morphology of GO, ZnONRA and RGO/ZnONRA nanocomposites was examined by atomic force microscopy (AFM) and field emission scanning electron microscopy (FESEM), respectively. Figure 2a shows a representative AFM height image of GO sheets deposited on a mica substrate with a thickness of $\approx 1.1 \text{ nm}$ (inset), which is consistent with the characteristic thickness of a single-layer GO,^[33] signifying the high quality of the obtained GO. Figure 2b displays an array of densely packed and nearly vertically aligned ZnO nanorods grown on the Fe–Co–Ni substrate. The average diameter and length of ZnO nanorods were about 100 nm and 3 μm (cross-sectional view; inset in Figure 2b), respectively. The FESEM images of ZnONRA covered by ultrathin RGO sheets produced at different concentrations of GO (i.e., yielding RGO/ZnONRA nanocomposites; see the Experimental Section) are shown in Figure 2c–f. At low GO concentration ($c = 0.5 \text{ mg mL}^{-1}$), transparent and discontinued islands of RGO sheets formed on the surface of ZnONRA was observed (Figure 2c). As the RGO content increased, large, transparent and continuous RGO sheets covered nearly entire surface of ZnONRA is clearly evident (Figure 2d). Obviously, the higher coverage may result in the better contact between RGO and ZnONRA, which is advantageous in improving the photocatalytic property of ZnO. However, as the GO concentration increased to 8 mg mL^{-1} (i.e., forming RGO/ZnONRA-3 nanocomposites), the ZnONRA was fully covered by the RGO sheets and it is

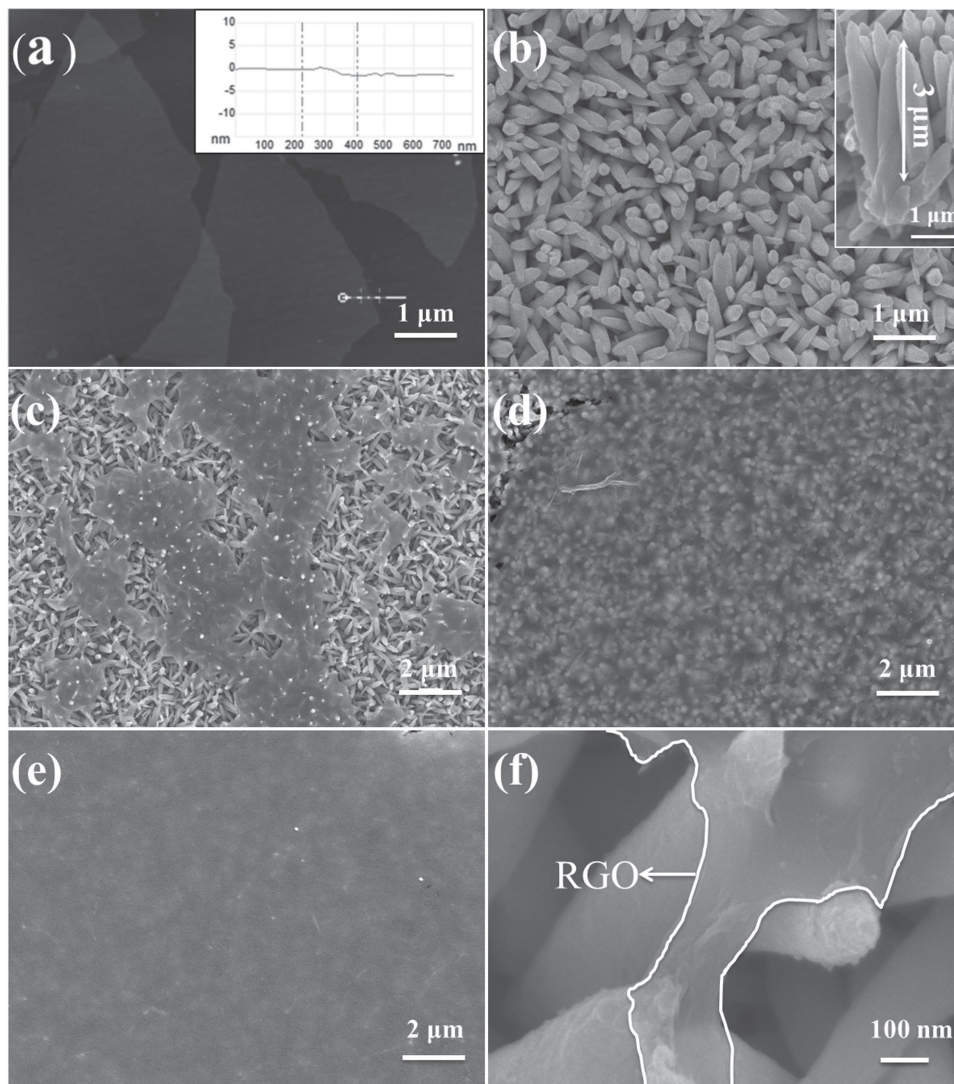


Figure 2. a) AFM image and the corresponding high profile (inset) of GO. FESEM images (top views) of b) ZnONRA, c) RGO/ZnONRA-1 ($c = 0.5 \text{ mg mL}^{-1}$), d, f) RGO/ZnONRA-2 ($c = 2 \text{ mg mL}^{-1}$), and e) RGO/ZnONRA-3 ($c = 8 \text{ mg mL}^{-1}$). The cross section of ZnONRA is shown as an inset in (b). The presence of RGO is marked with white lines in (f).

difficult to clearly see ZnO nanorods under the RGO sheet (Figure 2e), implying that the thickness of RGO increased. Clearly, the concentration of the GO solution played an important role in the final morphology of RGO/ZnONRA nanocomposites, which markedly affected their photocatalytic performance as discussed below. Figure 2f shows a close-up morphology of RGO/ZnONRA nanocomposites, confirming that thin RGO sheets covered on the surface of ZnO nanorods and also suggesting the good interfacial contact between RGO and ZnONRA facilitated by Sn^{2+} (see the Experimental Section). Furthermore, the deposition of RGO had no significant influence on the morphology of ZnONRA as the size and morphology of ZnO nanorods in the resulting RGO/ZnONRA nanocomposites (Figure 2f) were similar to ZnONRA prior to the RGO deposition.

The chemical composition and the state of elements on the surface of RGO/ZnONRA nanocomposites were scrutinized by X-ray photoelectron spectroscopy (XPS). The total survey spectrum showed the presence of Zn, O, and C

in RGO/ZnONRA nanocomposites (Figure 3a). The high-resolution XPS spectra of the Zn, O, and C elements were shown in Figure 3b–d, respectively. Two peaks centered at 1021.7 and 1045.1 eV in the Zn 2p spectrum can be assigned to the Zn 2p_{3/2} and Zn 2p_{1/2}, respectively (Figure 3b), corresponding to the states of Zn in ZnO. Figure 3c shows the O 1s spectrum, and two O 1s peaks were obtained using the multiplex-fitting procedure. The lower energy of 531.1 eV can be attributed to the Zn–O bonding. The peak at 533.5 eV can be assigned to the carboxyl groups, indicating that RGO contained a small amount of carboxyl groups. The efficient reduction of GO to RGO via Sn^{2+} was confirmed by the C1s spectrum (Figure 3d). The strong C1s peak at 284.6 eV and the weak binding energy peaks centered at 285.8, 287.6, and 289.1 eV can be assigned to the C–C bonding and C–OH, C=O, and OH–C=O functional groups, respectively,^[34] signifying a high-degree reduction of RGO in nanocomposites.^[35]

Figure 4a compares the Fourier transform infrared (FTIR) spectra of GO and RGO/ZnONRA nanocomposites

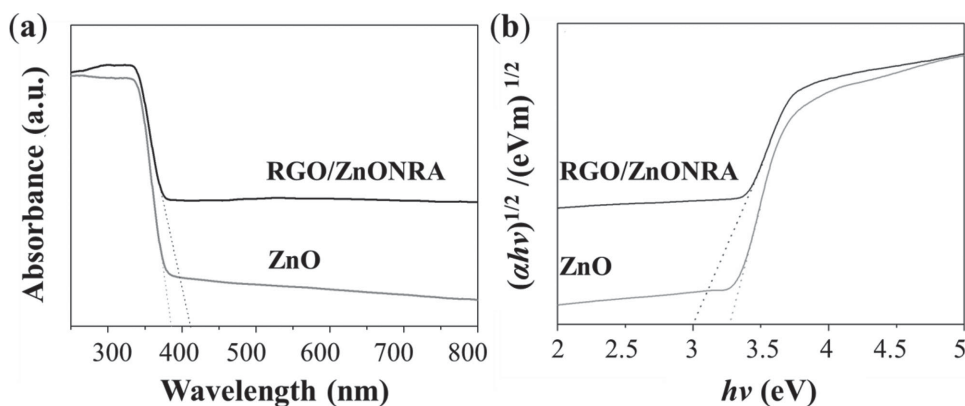


Figure 5. a) UV-vis diffuse reflectance spectra, and b) the bandgap evaluation from the $(\alpha hv)^{1/2}$ -photon-energy plots for ZnONRA and RGO/ZnONRA nanocomposites (i.e., RGO/ZnONRA-2), respectively.

which is larger than that in GO ($I_D/I_G = 1.00$), indicating that the structural defects in GO were slightly increased during the reduction process.

The UV-vis diffuse reflectance spectra (DRS) of ZnONRA and RGO/ZnONRA nanocomposites (i.e., RGO/ZnONRA-2) are shown in Figure 5a. Obviously, draping RGO over the surface of ZnONRA resulted in a variation on the optical property of ZnONRA. A red shift in the absorption edge and an improved absorption in the visible-light range are clearly evident, which may be ascribed to the formation of chemical bonding between RGO and ZnO.^[39] The optical bandgap energies, E_g , of ZnO and RGO/ZnONRA-2 were estimated according to the Kubelka-Munk equation.^[40,41] Figure 5b displays that E_g of ZnONRA is ≈ 3.3 eV and E_g of RGO/ZnONRA-2 was slightly reduced to 3.0 eV. The narrowing of the bandgap may be due likely to the chemical bonding between ZnO and RGO, that is, the formation of Zn—O—C bond, similar to the case of ZnO/carbon nanotube composites.^[42] Taken together, the extended light absorption range (corresponding to the reduced bandgap) and the enhanced visible-light absorption can be achieved, thereby leading to a potentially more efficient utilization of the solar spectrum.

Thus, the RGO/ZnONRA nanocomposites were employed in photocatalytic degradation of organic pollutants

under the visible-light irradiation. As a typical probe molecule, Rhodamine B (RhB) was selected for the photocatalytic reaction (see the Experimental Section). The degradation of RhB by the RGO/ZnONRA nanocomposites was conducted under the visible-light irradiation ($\lambda > 420$ nm). Figure 6a compares the visible-light photodegradation of RhB without the use of photocatalyst, with ZnONRA, three RGO/ZnONRA nanocomposites (i.e., RGO/ZnONRA-1, RGO/ZnONRA-2, and RGO/ZnONRA-3), and commercially available P25. The degradation efficiency is defined as C/C_0 , where C and C_0 are the remnant and initial concentration of RhB, respectively. As expected, the self-degradation of RhB (no photocatalyst) was nearly unnoticeable after visible-light exposure for 180 min, reflecting the high stability of RhB. When using commercial P25 and ZnONRA as the photocatalysts, the concentration of RhB was slightly decreased by 13.6% and 18.6%, respectively, after 180 min. This is not surprising as TiO_2 and ZnO cannot be effectively excited by visible light due to their wide bandgaps. In sharp contrast, it is clear that all three RGO/ZnONRA nanocomposites photocatalysts exhibited the remarkably higher photocatalytic activities than P25 and ZnONRA, substantiating that the modification of ZnONRA with RGO can markedly improve its visible-light photocatalytic property, even at a relatively low content of RGO (i.e., RGO/ZnONRA-1). Particularly, the RGO/ZnONRA-2

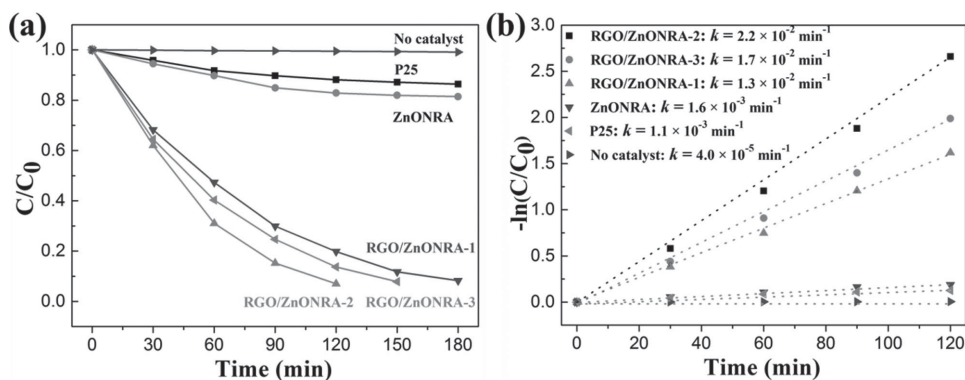


Figure 6. a) Photocatalytic degradation profiles of RhB by employing three different RGO/ZnONRA nanocomposites (i.e., RGO/ZnONRA-1 ($c = 0.5$ mg mL⁻¹), RGO/ZnONRA-2 ($c = 2$ mg mL⁻¹), and RGO/ZnONRA-3 ($c = 8$ mg mL⁻¹), ZnONRA, P25, and no photocatalyst, respectively, and b) the corresponding pseudo-first-order kinetic plots.

sample yielded the highest photocatalytic efficiency among all tested photocatalysts, that is, 93.5% of RhB was degraded by RGO/ZnONRA-2 within a 2 h visible-light irradiation. The decomposition of RhB can be fitted to a pseudo-first-order kinetics, $-\ln(C/C_0) = kt$, where t is the light irradiation time and k is the photocatalytic reaction apparent rate constant. Figure 6b depicts the effect of different photocatalysts on the kinetics of RhB under the visible-light illumination. The k for the RGO/ZnONRA-2, RGO/ZnONRA-3, RGO/ZnONRA-1, ZnONRA, and P25 were calculated to be 2.2×10^{-2} , 1.7×10^{-2} , 1.3×10^{-2} , 1.6×10^{-3} and $1.1 \times 10^{-3} \text{ min}^{-1}$, respectively. It is important to note that the photocatalytic degradation rate of RGO/ZnONRA-2 was 14-fold and 20-fold higher than that of ZnONRA and P25, respectively. The k of RGO/ZnONRA-2 and RGO/ZnONRA-3 were slightly higher than that of RGO/ZnONRA-1 due largely to the presence of more interfacial contact between ZnONRA and RGO sheets, as evidenced by the SEM measurements (Figure 2). Notably, the visible-light photocatalytic performance of RGO/ZnONRA-3 was lower than that of RGO/ZnONRA-2, suggesting that the high content of RGO in the RGO/ZnONRA-3 nanocomposites did not afford an improved photocatalytic performance. This observation can be rationalized as follows. On one hand, the high content of RGO cannot result in additional effective interfacial contact with ZnONRA as the nearly full surface coverage of RGO was already realized when the concentration of GO was 2 mg mL^{-1} (i.e., RGO/ZnONRA-2; Figure 2d). On the other hand, the thicker RGO sheets in RGO/ZnONRA-3 may lead to the blocking of the active areas of nanocomposite materials from the visible-light exposure.^[43,44]

As the photocatalytic performance is closely related to the separation of photogenerated charges, the separation of electrons and holes was evaluated by measuring the photocurrent of ZnONRA before and after the introduction of RGO. The photoresponses of as-prepared photoelectrodes were measured with the light on/off cycles at 0 V versus the saturated calomel electrode (Figure 7a). We note that uniform and fast photocurrent responses were observed for each light-on and light-off cycle for all photoelectrodes, indicating that the charge separation in the photoelectrodes proceeded very quickly. In comparison with the ZnONRA, the RGO/ZnONRA-2 photoelectrode showed a significantly increased photocurrent. The maximum photocurrent density of RGO/ZnONRA-2 reached

$22.5 \mu\text{A cm}^{-2}$, which is five times higher than that of ZnONRA of $4.3 \mu\text{A cm}^{-2}$. The enhanced photocurrent response suggested the efficient electron separation in the RGO/ZnONRA nanocomposites, which is crucial for the enhanced photocatalytic performance. Moreover, the electrochemical impedance spectroscopy (EIS) measurements were also performed to determine the improved charge separation of RGO/ZnONRA nanocomposites. The Nyquist plots of ZnONRA and RGO/ZnONRA-2 under the visible-light illumination are shown in Figure 7b. The radius of the semicircle is related to the reaction rate occurring at the surface of the catalytic electrodes. Compared to ZnONRA, RGO/ZnONRA-2 showed a depressed semicircle, suggesting a more effective charge separation process after the introduction of RGO.

In addition to the photocatalytic activity, the stability of photocatalysts are also important for their practical applications. In contrast to the common photocatalysts existed in the form of dispersed nanoparticles in the reaction media, the RGO/ZnONRA nanocomposites were directly deposited on the Fe-Co-Ni substrate. Thus, they can be conveniently reused for multiple photocatalytic processes without the tedious centrifugation process often encountered in copious previous work. To investigate the stability of photocatalytic performance in visible-light region, the RGO/ZnONRA-2 was employed to degrade RhB in five consecutive cycles as shown in Figure 8. Prior to each experiment, the used photocatalyst was rinsed with deionized water. Despite a slight loss of photocatalytic activity (within 5%), the RGO/ZnONRA-2 nanocomposites maintained a high photocatalytic activity even after the fifth reaction cycle, reflecting the outstanding stability of RGO/ZnONRA nanocomposites. Such superior stability may be resulted from the effective coverage of ZnONRA by RGO which prevented the photocorrosion of ZnO during the photocatalytic process and in turn led to the improved stability.

In the following we turn our attention to the possible mechanism for the markedly enhanced visible-light photocatalytic activity in RGO/ZnONRA nanocomposites. ZnO is known as a wide bandgap semiconductor (3.37 eV) and cannot be photoexcited under the visible-light irradiation. However, the judicious deposition of RGO sheets over ZnONRA rendered the visible-light photocatalytic activity of the resulting RGO/ZnONRA nanocomposites. RGO is a zero-bandgap

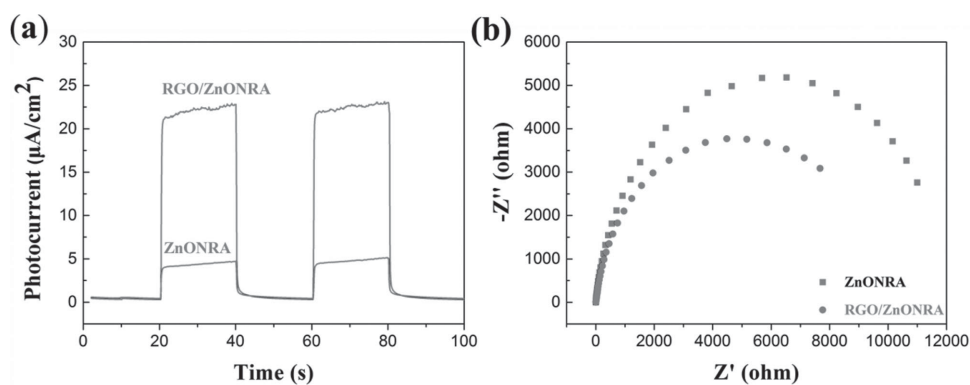


Figure 7. a) Photoresponse profiles and b) Nyquist impedance plots of pure ZnONRA and RGO/ZnONRA nanocomposites (RGO/ZnONRA-2), respectively.

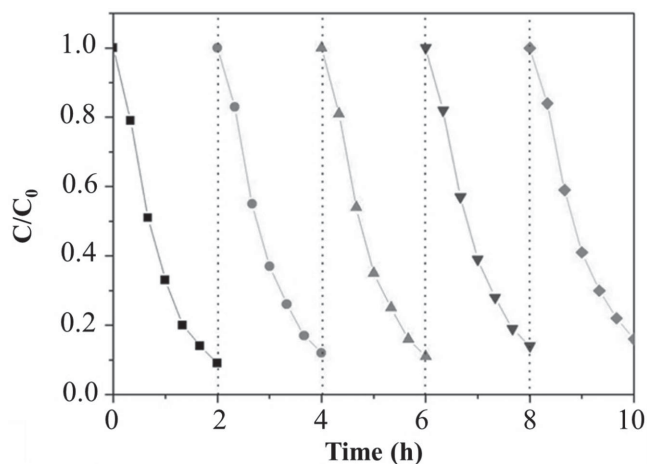


Figure 8. Cycling performance of RGO/ZnONRA nanocomposites (i.e., RGO/ZnONRA-2) in the photocatalytic degradation of RhB under visible-light irradiation.

semiconductor with a work function of -4.42 eV ^[45] and can be excited under the visible-light irradiation as proven by calculations and experiments.^[46–48] One possible scenario for the generation of photoelectrons in RGO/ZnONRA under visible-light irradiation is the photoexcitation of RGO, as illustrated in **Scheme 1a**. During the photocatalytic process, RGO is first excited from the ground state RGO to the excited state RGO*, generating photoelectrons. Due to the excellent electron conductivity of RGO, the high electron mobility of ZnONRA, and the efficient interfacial contact between RGO and ZnONRA, these photoelectrons can rapidly inject into the conduction band (CB) of ZnO. The electrons react with oxygen dissolved in water to form the activated superoxide radical anion $\bullet\text{O}_2^-$ which can subsequently transform into $\bullet\text{OH}$ radicals as represented in Equations (1)–(3)



Both $\bullet\text{O}_2^-$ and $\bullet\text{OH}$ are strong oxidants that degrade RhB. Thus, we propose that during the visible-light photocatalytic process for RGO/ZnONRA nanocomposites, RGO acts as a photosensitizer to generate photoelectrons, rather than as electrons acceptor. In addition, it has been demonstrated

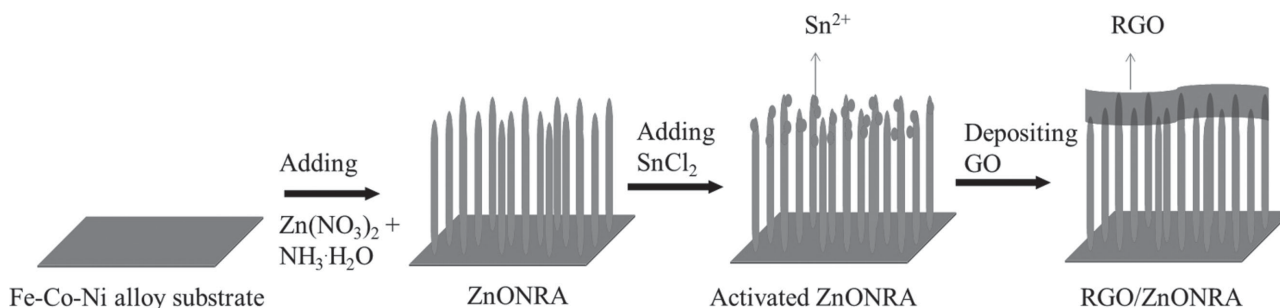
that the dyes can sensitize the wide bandgap semiconductors, making them suitable for utilizing visible photons.^[49] In this work, RhB can thus function as a photosensitizer as well to generate photoelectrons under the visible-light irradiation.^[50] As depicted in Scheme 1b, the work function of RhB* is -3.08 eV , which is higher than that of RGO (-4.42 eV). Most of dyes are attached to the surface of RGO due to the large surface area of RGO. Therefore, the photo-induced electrons can be favorably transferred from RhB* to RGO, and injected into the CB of ZnO. We speculate that these two scenarios (i.e., cophotosensitizations by RGO and RhB) collectively impart the visible-light photocatalytic degradation of RGO/ZnONRA nanocomposites with markedly enhanced performance over ZnONRA.

3. Conclusions

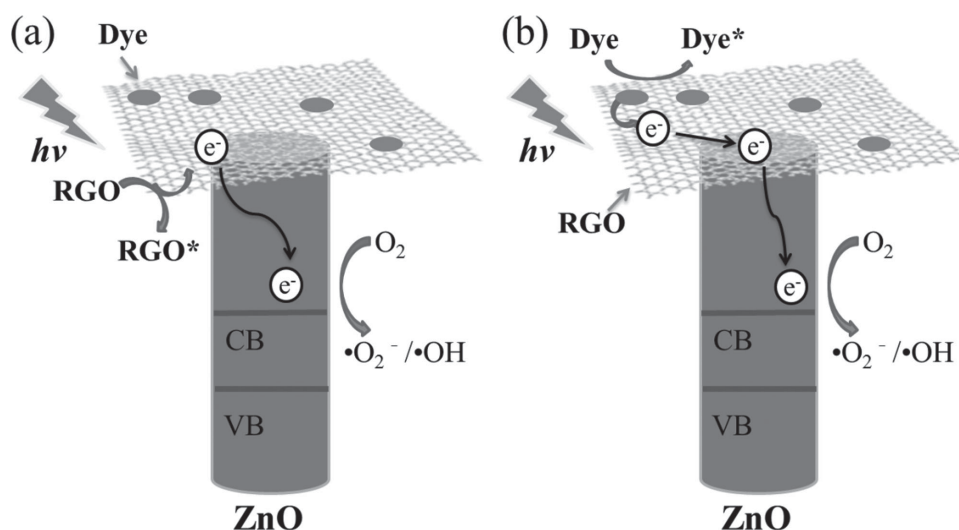
In summary, RGO/ZnONRA nanocomposites with high visible-light photocatalytic performance were successfully produced via a surprisingly simple wet-chemistry approach. The amount of RGO draped over ZnONRA exerted a notable influence on the photocatalytic activity of RGO/ZnONRA nanocomposites. The highest photocatalytic degradation rate of RGO/ZnONRA on RhB was 14 times higher than that of ZnONRA alone. The nanocomposites also exhibited an outstanding stability due to the surface protection by RGO. This simple yet effective strategy can be readily extended to produce other RGO-decorated wide bandgap semiconductor nanocomposites for the better visible-light utilization with promising potential for applications in the oxidative decomposition of organic pollutants, hydrogen generation, nanogenerator, and solar cells.

4. Experimental Section

Preparation of RGO/ZnONRA: As shown in **Scheme 2**, ZnO nanorod arrays (ZnONRA) were prepared on the alloyed Fe–Co–Ni substrate via a facile one-step approach.^[51,52] Notably, a seed layer was not needed, which simplified the preparation process. In a typical synthesis, a piece of the Fe–Co–Ni substrate ($20 \times 20 \times 0.15\text{ mm}^3$) was cleaned in the ultrasonic bath with absolute ethanol and deionized water. Subsequently, the substrate was suspended in 200 mL of aqueous solution containing $\text{Zn}(\text{NO}_3)_2$ (0.035 M) and $\text{NH}_3 \cdot \text{H}_2\text{O}$ (0.65 M) in a sealed beaker followed by heating at a constant temperature of $70\text{ }^\circ\text{C}$ for 24 h. After the reaction, the substrate tightly covered with ZnO nanorod arrays was

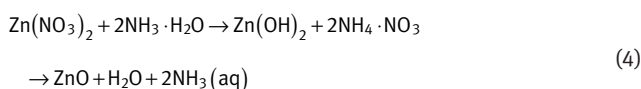


Scheme 1. Schematic illustration of the facile synthesis of RGO/ZnONRA nanocomposites.



Scheme 2. Proposed mechanisms for the photocatalytic degradation of RhB by capitalizing on RGO/ZnONRA nanocomposites as photocatalyst under the visible-light irradiation.

rinsed with ethanol and dried in air at room temperature. The chemical reaction for the growth of ZnO nanorods is given as follows



The GO was prepared from natural graphite by the improved Hummers method.^[33] The RGO sheets were deposited on the surface of ZnONRA by a simple wet-chemistry approach. First, as-prepared ZnONRA was carefully immersed into 50 mL SnCl_2 ethanol solution (0.05 M) with vigorous stirring for about 30 min at room temperature to obtain the Sn^{2+} -activated ZnONRA. Subsequently, an optimized amount of GO was uniformly dispersed in distilled water (200 mL) by ultrasonication for 30 min. The film with the Sn^{2+} -activated ZnONRA was then immersed into the GO solution and stirred for 1 h at 70 °C. It is noteworthy that GO with $-\text{OH}$ and $-\text{COOH}$ on the surface can be easily attached on the surface of Sn^{2+} -activated ZnONRA due to the electrostatic adsorption with Sn^{2+} , and was then reduced to RGO by Sn^{2+} . After that, the obtained RGO/ZnONRA nanocomposites were removed from the solution and washed with deionized water for several times. The formed SnO_2 particles were washed off by water during this process, which was confirmed by XRD measurement on the products. As RGO sheets were well-spread out on the surface of ZnONRA over a large area and a large quantity of interfacial contacts were formed between them, the RGO sheets sustained the water washing. Finally, the products were dried in a vacuum oven at 60 °C overnight.

In our study, the amount of RGO deposited on the surface of ZnONRA can be readily tuned by varying the concentration of GO. Accordingly, the resulting RGO/ZnONRA nanocomposites were referred to as RGO/ZnONRA-1 (the concentration of GO, $c = 0.5 \text{ mg mL}^{-1}$), RGO/ZnONRA-2 ($c = 2 \text{ mg mL}^{-1}$), and RGO/ZnONRA-3 ($c = 8 \text{ mg mL}^{-1}$).

Characterization: The XRD measurements were performed on a Dmax-3 β diffractometer with nickel-filtered Cu K α radiation ($\lambda = 1.54178 \text{ \AA}$). The XPS was collected on the ESCALab MKII X-ray photoelectron spectrometer (K-Alpha 1063). The size and morphology of the samples were investigated by FESEM (JEOL-6300F). FTIR

reflectance spectra were recorded on a FD-5DX FTIR spectrometer. Raman spectra were recorded at room temperature using a micro-Raman spectrometer (InVia, Renishaw plc, Gloucestershire, UK) in the backscattering geometry with a 514.5 nm Ar⁺ laser as an excitation source. The UV-vis DRS were obtained using a Lambda 35 UV-vis spectrometer.

Photocatalytic Measurements: The photocatalytic activities of as-prepared samples were evaluated by degrading RhB under the visible-light irradiation. A 500 W xenon lamp with an ultraviolet filter was used as a light source and the distance between the samples was 8 cm. In a typical measurement, the films with an effective area of $2 \times 2 \text{ cm}^2$ were horizontally immersed in 30 mL of 10 mg L^{-1} RhB solution in a quartz reactor. Prior to illumination, the suspension was magnetically stirred in the dark for 1 h to ensure the adsorption/desorption equilibrium of RhB with the RGO/ZnONRA nanocomposites photocatalysts. Afterward, the solution was stirred incessantly under the visible light and the temperature was maintained at room temperature using circulating water. The concentration of RhB was measured by a UV-2401 spectrophotometer for every 30 min.

Photoelectrochemical Measurements: The photoelectrochemical characteristics of samples were measured using an electrochemical workstation (CHI660C, Chenhua, China) with a three-electrode system, which was operated with the RGO/ZnONRA films as the working electrode, the platinum wire as the counter electrode, and the Ag/AgCl as the reference electrode. The working electrode was irradiated by a 500 W xenon lamp with a 420 nm cutoff filter. The measurements were carried out in 0.1 M Na_2SO_4 aqueous solution. The EIS over a frequency range from 0.01 Hz to 100 kHz at the open-circuit voltage was conducted on the same electrochemical workstation.

Acknowledgements

X.Q.L. and J.B.Y. contributed equally to this work. This work was supported by the Fund for Outstanding Doctoral Dissertation of China University of Geosciences, the financial support from the Chinese

Scholarship Council, National Natural Science Foundation of China (21201156), and the Fundamental Research Funds for National University, China University of Geosciences (Wuhan, CUG130401).

- [1] D. Liu, T. L. Kelly, *Nat. Photonics* **2014**, *8*, 133.
- [2] C. Tian, Q. Zhang, A. Wu, M. Jiang, Z. Liang, B. Jiang, H. Fu, *Chem. Commun.* **2012**, *48*, 2858.
- [3] J. Xu, Z. Chen, J. A. Zapfen, C. S. Lee, W. Zhang, *Adv. Mater.* **2014**, *26*, 5337.
- [4] X. Xin, H. Y. Liu, M. Ye, Z. Lin, *Nanoscale* **2013**, *5*, 11220.
- [5] B. Nikoobakht, X. Wang, A. Herzog, J. Shi, *Chem. Soc. Rev.* **2013**, *42*, 342.
- [6] Y. K. Park, W. Y. Rho, T. Mahmoudi, Y. B. Hahn, *Chem. Commun.* **2014**, *50*, 10502.
- [7] Y. Wei, C. Xu, S. Xu, C. Li, W. Wu, Z. L. Wang, *Nano Lett.* **2010**, *10*, 2092.
- [8] T. H. Yang, L. D. Huang, Y. W. Harn, C. C. Lin, J. K. Chang, C. I. Wu, J. M. Wu, *Small* **2013**, *9*, 3169.
- [9] C. Han, Z. Chen, N. Zhang, J. C. Colmenares, Y.-J. Xu, *Adv. Funct. Mater.* **2015**, *25*, 221.
- [10] J. Liu, Y. Li, R. Ding, J. Jiang, Y. Hu, X. Ji, Q. Chi, Z. Zhu, X. Huang, *J. Phys. Chem. C* **2009**, *113*, 5336.
- [11] Y. Yang, C. Han, B. Jiang, J. Iocozzia, C. He, D. Shi, T. Jiang, Z. Lin, *Mater. Sci. Eng. R* **2016**, *102*, 1.
- [12] Y. Sang, Z. Zhao, J. Tian, P. Hao, H. Jiang, H. Liu, J. P. Claverie, *Small* **2014**, *10*, 3775.
- [13] L. Sun, Y. Bai, N. Zhang, K. Sun, *Chem. Commun.* **2015**, *51*, 1846.
- [14] Y. Yang, W. Zhan, R. Peng, C. He, X. Pang, D. Shi, T. Jiang, Z. Lin, *Adv. Mater.* **2015**, *27*, 6376.
- [15] S. Wu, R. Xu, M. Lu, R. Ge, J. Iocozzia, C. Han, B. Jiang, Z. Lin, *Adv. Energy Mater.* **2015**, *5*, 1500400.
- [16] J.-J. Chen, Q. Wang, J. Meng, X. Ke, G. V. Tendeloo, Y.-Q. Bie, J. Liu, K. Liu, Z.-M. Liao, D. Sun, *ACS Nano* **2015**, *9*, 8851.
- [17] M.-Q. Yang, Y.-J. Xu, *J. Phys. Chem. C* **2013**, *117*, 21724.
- [18] A. Bhirud, S. Sathaye, R. Waichal, C.-J. Park, B. Kale, *J. Mater. Chem. A* **2015**, *3*, 17050.
- [19] S. Y. Sawant, M. H. Cho, *RSC Adv.* **2015**, *5*, 97788.
- [20] B. Li, H. Cao, *J. Mater. Chem.* **2011**, *21*, 3346.
- [21] T. Xu, L. Zhang, H. Cheng, Y. Zhu, *Appl. Catal., B* **2011**, *101*, 382.
- [22] X. Liu, L. Pan, T. Lv, T. Lu, G. Zhu, Z. Sun, C. Sun, *Catal. Sci. Technol.* **2011**, *1*, 1189.
- [23] V. Q. Dang, T. Q. Trung, D. I. Kim, T. Duy le, B. U. Hwang, D. W. Lee, B. Y. Kim, D. Toan le, N. E. Lee, *Small* **2015**, *11*, 3054.
- [24] H. Park, S. Chang, J. Jean, J. J. Cheng, P. T. Araujo, M. Wang, M. G. Bawendi, M. S. Dresselhaus, V. Bulovic, J. Kong, S. Gradecak, *Nano Lett.* **2013**, *13*, 233.
- [25] Z. Yin, S. Wu, X. Zhou, X. Huang, Q. Zhang, F. Boey, H. Zhang, *Small* **2010**, *6*, 307.
- [26] S. Ameen, M. S. Akhtar, M. Song, H. S. Shin, *ACS Appl. Mater. Interfaces* **2012**, *4*, 4405.
- [27] J. Chen, C. Li, G. Eda, Y. Zhang, W. Lei, M. Chhowalla, W. I. Milne, W. Q. Deng, *Chem. Commun.* **2011**, *47*, 6084.
- [28] B. D. Boruah, A. Mukherjee, S. Sridhar, A. Misra, *ACS Appl. Mater. Interfaces* **2015**, *7*, 10606.
- [29] H. Liu, Q. Sun, J. Xing, Z. Zheng, Z. Zhang, Z. Lu, K. Zhao, *ACS Appl. Mater. Interfaces* **2015**, *7*, 6645.
- [30] J. Liu, R. Lu, G. Xu, J. Wu, P. Thapa, D. Moore, *Adv. Funct. Mater.* **2013**, *23*, 4941.
- [31] J. Liu, H. Bai, Y. Wang, Z. Liu, X. Zhang, D. D. Sun, *Adv. Funct. Mater.* **2010**, *20*, 4175.
- [32] Z. Zheng, Z. S. Lim, Y. Peng, L. You, L. Chen, J. Wang, *Sci. Rep.* **2013**, *3*, 2434.
- [33] D. C. Marcano, D. V. Kosynkin, J. M. Berlin, A. Sinitskii, Z. Sun, A. Slesarev, L. B. Alemany, W. Lu, J. M. Tour, *ACS Nano* **2010**, *4*, 4806.
- [34] C. Xu, X. Wang, J. Zhu, *J. Phys. Chem. C* **2008**, *112*, 19841.
- [35] Y. Wen, H. Ding, Y. Shan, *Nanoscale* **2011**, *3*, 4411.
- [36] X. W. Fu, Z. M. Liao, R. Liu, J. Xu, D. Yu, *ACS Nano* **2013**, *7*, 8891.
- [37] S. Z. Deng, H. M. Fan, M. Wang, M. R. Zheng, J. B. Yi, R. Q. Wu, H. R. Tan, C. H. Sow, J. Ding, Y. P. Feng, *ACS Nano* **2009**, *4*, 495.
- [38] M. Šćepanović, M. Grujić-Brojčin, K. Vojisavljević, S. Bernik, T. Srečković, *J. Raman Spectrosc.* **2010**, *41*, 914.
- [39] Y. Zhang, Z. R. Tang, X. Fu, Y. J. Xu, *ACS Nano* **2010**, *4*, 7303.
- [40] H. S. Kim, C. R. Lee, J. H. Im, K. B. Lee, T. Moehl, A. Marchioro, S. J. Moon, R. Humphry-Baker, J. H. Yum, J. E. Moser, M. Gratzel, N. G. Park, *Sci. Rep.* **2012**, *2*, 591.
- [41] X. Liu, Z. Li, W. Zhao, C. Zhao, Y. Wang, Z. Lin, *J. Mater. Chem. A* **2015**, *3*, 19148.
- [42] T. Lv, L. Pan, X. Liu, Z. Sun, *Catal. Sci. Technol.* **2012**, *2*, 2297.
- [43] Z. Chen, N. Zhang, Y. J. Xu, *CrystEngComm* **2013**, *15*, 3022.
- [44] L. Xu, F. Zhang, X. Song, Z. Yin, Y. Bu, *J. Mater. Chem. A* **2015**, *3*, 5923.
- [45] Z. Xiong, L. L. Zhang, J. Ma, X. S. Zhao, *Chem. Commun.* **2010**, *46*, 6099.
- [46] X. Xie, K. Kretschmer, G. Wang, *Nanoscale* **2015**, *7*, 13278.
- [47] Y. Zhang, N. Zhang, Z. R. Tang, Y. J. Xu, *ACS Nano* **2012**, *6*, 9777.
- [48] A. Du, Y. H. Ng, N. J. Bell, Z. Zhu, R. Amal, S. C. Smith, *J. Phys. Chem. Lett.* **2011**, *2*, 894.
- [49] D. Chatterjee, S. Dasgupta, *J. Photochem. Photobiol., C* **2005**, *6*, 186.
- [50] J. Yu, S. Zhuang, X. Xu, W. Zhu, B. Feng, J. Hu, *J. Mater. Chem. A* **2015**, *3*, 1199.
- [51] X. Liu, Z. Li, W. Zhao, C. Zhao, J. Yang, Y. Wang, *J. Colloid Interface Sci.* **2014**, *432*, 170.
- [52] J. Liu, X. Huang, Y. Li, X. Ji, Z. Li, X. He, F. Sun, *J. Phys. Chem. C* **2007**, *111*, 4990.

Received: March 31, 2016
Revised: May 17, 2016
Published online: June 20, 2016